Check for updates

A bimetallic strategy to modulate electronic metal support interaction in Co_3O_4(111)-based catalysts: the case of supported Rh–Pt core–shell nanoparticles

Jonas Hauner, [ID][a] Alexander Simanenko, [ID][a] Lukáš Fusek, [ID][b] Tomáš Skála, [ID][b] Nataliya Tsud, [ID][b] Firas Faisal, [ID][a] Sascha Mehl, [ID][c] Jörg Libuda [ID][a] and Yaroslava Lykhach [ID] *[a]

The electronic metal support interaction (EMSI) plays a decisive role in determining the activity, selectivity, and stability of noble metal catalysts supported on reducible oxides. While EMSI can enhance catalytic performance, excessively strong charge transfer at the metal/oxide interface often leads to oxidation and disintegration of metal nanoparticles, particularly in systems such as Rh/Co_3O_4(111). In this work, we explore how bimetallic Rh–Pt interactions modulate and counteract EMSI at the Rh/Co_3O_4(111) interface. Two types of core–shell Rh–Pt nanoparticles with precisely controlled compositions and architectures were prepared on well-ordered Co_3O_4(111) thin films on an Ir(100) substrate and investigated using synchrotron radiation photoelectron spectroscopy. We found that incorporating Pt, either as the core in Pt@Rh or as the shell in Rh@Pt nanoparticles, significantly attenuates charge transfer, thereby stabilizing Rh in its metallic state and suppressing disintegration of the core@shell nanoparticles. This stabilization is attributed to strong Rh–Pt interaction and the ability of the two metals to form stoichiometric binary phases. These findings demonstrate that bimetallic interactions offer an effective strategy to tune EMSI, providing a fundamental basis for the design of electronically balanced and thermally stable catalysts supported on reducible oxides.

1. Introduction

The electronic metal support interaction (EMSI) has emerged as a powerful strategy to optimize catalytic activity and selectivity of noble metal nanoparticles supported on reducible oxides.[1–3] This phenomenon arises from charge transfer across the metal/oxide interface, leading to partial oxidation or reduction of the noble metal nanoparticles and, correspondingly, partial reduction or oxidation of the oxide support.[4,5] The magnitude of EMSI is primarily governed by the electronic properties of both the reducible oxide and the supported noble metal, namely by work function differences.[5–9] In the well-studied case of CeO_2(111)-based catalysts, noble metal nanoparticles retain their metallic character.[4,9,10] However, under specific conditions, these nanoparticles can disintegrate into isolated atoms.[11,12] Such conditions may occur due to defect formation induced by nanostructuring,[11] or may intrinsically exist on the defect-free, cation-terminated surfaces of reducible oxides such as Fe_2O_3, Fe_3O_4, and Co_3O_4.[13–17] In these systems, noble metal atoms substitute surface cations, adopting their local coordination environments. Such surface modifications can be exploited to enhance electrocatalytic activity in Co_3O_4 – based materials, taking advantage of the intrinsic stability of Co_3O_4 in alkaline electrolytes.[18]

Previously, we demonstrated that deposition of sub-monolayer Pt on Co_3O_4(111) results in partial substitution of Co^{2+} by Pt^{2+} cations.[17] Upon annealing, Pt atoms migrate into the subsurface region, substituting Co^{3+} and forming Pt^{4+} species. A similar phenomenon occurs for Rh, although the extent of Rh nanoparticle disintegration and oxidation under ultrahigh vacuum (UHV) annealing is markedly greater.[19] Such strong EMSI can be detrimental in catalytic systems where maintaining the metallic character of Rh nanoparticles is crucial, *e.g.*, in electrocatalysis.[20]

Developing strategies to mitigate or modulate EMSI is therefore essential for the rational design of stable, high-performance catalysts.[3,6,21] Several approaches have been proposed, including

[a] Interface Research and Catalysis, ECRC, Friedrich-Alexander-Universität Erlangen-Nürnberg, Egerlandstrasse 3, 91058 Erlangen, Germany. E-mail: yaroslava.lykhach@fau.de

[b] Charles University, Faculty of Mathematics and Physics, Department of Surface and Plasma Science, V Holešovičkách 2, Prague, 18000, Czech Republic

[c] Elettra-Sincrotrone Trieste SCpA, Strada Statale 14, km 163.5, Basovizza-Trieste, 34149, Italy

This journal is © the Owner Societies 2026

Phys. Chem. Chem. Phys., 2026, **28**, 3675–3681 | 3675

(i) tuning the electronic structure of the oxide support by doping or introducing oxygen vacancies,[3,8,9,21,22] (ii) controlling the size of the supported nanoparticles,[3,4,9] and (iii) tailoring the composition and nanostructure of the supported nanoparticles by introducing a second metal.[3] Among these, the introduction of bimetallic interactions has emerged as an especially promising approach. The presence of a second metal can alter the electronic structure of the active phase, redistribute charge at the metal/oxide interface, and thus counterbalance excessive EMSI.

In our earlier work on bimetallic Rh–Pd core–shell nanoparticles supported on $Co_3O_4(111)$,[19] we found that the Rh–Pd interaction was too weak to stabilize the metallic core–shell nanostructure. Upon annealing in UHV, the Rh–Pd core–shell nanoparticles readily disintegrated into separate Rh and Pd particles.

In the present study, we investigate the effect of bimetallic interactions in Rh–Pt nanoparticles supported on $Co_3O_4(111)$. In contrast to palladium, Pt exhibits stronger metal–metal bonding with Rh, yielding bimetallic phases,[23–25] which is expected to mitigate charge transfer to the oxide. Using synchrotron radiation photoelectron spectroscopy (SRPES), we systematically examine the chemical state evolution and thermal stability of two types of Rh–Pt core–shell nanoparticles, Pt@Rh and Rh@Pt, supported on $Co_3O_4(111)$. Through careful analysis of core level binding energy shifts, surface composition changes, and temperature-dependent transformations, we elucidate how Rh–Pt bimetallic interactions influence charge redistribution at the $Rh/Co_3O_4(111)$ interface. Our results demonstrate that the incorporation of Pt into Rh nanoparticles can efficiently counterbalance the extent of charge transfer, preventing excessive oxidation of Rh and stabilizing the metallic phase under conditions that otherwise promote strong EMSI.

2. Experimental

SRPES experiments were performed at the Materials Science Beamline (MSB) of the Elettra synchrotron light facility in Trieste, Italy. The MSB was equipped with a bending magnet source and provided synchrotron light in the energy range of 22–1000 eV. The UHV end-station (base pressure 2×10^{-10} mbar) was equipped with a hemispherical electron energy analyzer (Specs Phoibos 150) with a delay-line detector, a dual Mg/Al X-ray source, a rear-view LEED optics, a sputter gun (Ar$^+$), and a gas inlet system. In addition, electron-beam evaporators for Co, Pt, and Rh metal deposition were installed.

The studies discussed below were performed using a surface science approach, which involves the preparation of Rh–Pt core–shell nanoparticles supported on a well-ordered $Co_3O_4(111)$ film grown on a bulk Ir(100) single crystal substrate. Characterization of the structure of such model systems is not compatible with techniques typically used for powder samples.[26]

The $Co_3O_4(111)$ film was prepared on an Ir(100) substrate using a multi-step procedure[27–29] that has been previously used in other works.[19,30] The sample temperature was controlled by a DC power supply passing a current through Ta wires holding the sample. The temperature was monitored by a K-type thermocouple spot-welded to the side of the sample. The Ir(100) single crystal (MaTecK, 99.99%) was first cleaned by several cycles of Ar$^+$ sputtering (300 K, 60 min), followed by annealing in UHV (3 min), then in an oxygen atmosphere (1×10^{-7} mbar, SIAD, 99.999%, 3 min), and again in UHV (3 min) at 1200 K until no traces of carbon or other impurities were found in the photoelectron spectra. Subsequent annealing of the Ir(100) crystal in an oxygen atmosphere (5×10^{-7} mbar, 1200 K, 5 min) yielded the (2×1)–O reconstruction. An epitaxial $Co_3O_4(111)$ film was then grown on the (2×1)–O/Ir(100) surface by physical vapor deposition (PVD) of Co metal (Goodfellow, 99.99%) in an oxygen atmosphere (2×10^{-6} mbar) at 273 K, followed by annealing in oxygen (2×10^{-6} mbar) at 523 K for 10 min and at 603 K for 7 min, followed by annealing in UHV at 603 K for 3 min and at 680 K for 3 min. This method yielded a continuous, stoichiometric $Co_3O_4(111)$ film with a thickness of 6.0 nm, as determined from the attenuation of the Ir 4f core level intensity. LEED observations on the prepared films confirmed the epitaxial growth of $Co_3O_4(111)$ (see SI, Fig. S1).

The bimetallic Rh–Pt core–shell nanoparticles were prepared by subsequent PVD of 0.5 ML of Pt and 0.5 ML of Rh metals or *vice versa* on $Co_3O_4(111)/Ir(100)$ at 300 K in UHV. We denote the resulting core–shell nanoparticles as Pt@Rh/$Co_3O_4(111)$ and Rh@Pt/$Co_3O_4(111)$ based on the broadly accepted definition for the core@shell nanoparticles, where the core is an inner metal and the shell is an outer metal.[31] The nominal thickness of the core metal was determined from the attenuation of the Co 2p core level intensity, while the nominal thickness of the shell metal was determined from the attenuation of the core level intensity of the core metal. The Pt and Rh thicknesses are expressed in terms of monolayers, ML, where 1 ML corresponds to 0.226 nm (Pt) and 0.219 nm (Rh). Additionally, two previously studied[19,32] monometallic Rh/$Co_3O_4(111)$ and Pt/$Co_3O_4(111)$ model catalysts were used as reference systems. Rh thickness in Rh/$Co_3O_4(111)$ was 1.9 ML and Pt thickness in Pt/$Co_3O_4(111)$ was 1.3 ML.

Core level spectra were acquired with photon energies of 180 eV (Pt 4f), 410 eV (C 1s, Rh 3d, Pt 4f), 650 eV (O 1s, Rh 3d, Pt 4f), 812 eV (Rh 3d), and 930 eV (Co 2p). Valence band spectra were acquired at a photon energy of 60 eV. All spectra were acquired with a constant pass energy and an emission angle of the photoelectrons of 0° with respect to the sample normal.

The total spectral resolutions were 200 meV (60 eV, 115 eV, and 180 eV), 350 meV (410 eV), 600 meV (650 eV), 800 meV (812 eV), and 1 eV (930 eV). The KolXPD fitting software was used to process the obtained data and analyze the spectra.[33] The spectral components in the Rh 3d and Pt 4f core level spectra were fitted with an asymmetric Doniach–Šunjić function convoluted with a Gaussian profile after subtraction of the Shirley background. The Rh 3d and Pt 4f core level spectra were fitted with a spin–orbit splitting of 4.7 eV and 3.3 eV, respectively. The Coster–Kronig effect, which leads to a broadening of the Rh $3d_{3/2}$ component compared to Rh $3d_{5/2}$, was considered. Specifically, the Rh 3d core levels were fitted with two asymmetric Doniach–Šunjić functions convoluted with a Gaussian profile.

3676 | *Phys. Chem. Chem. Phys.*, 2026, **28**, 3675–3681

This journal is © the Owner Societies 2026

The Co^{3+}/Co^{2+} concentration ratio was determined from the intensities of the corresponding Co^{3+} and Co^{2+} features in the valence band spectra obtained with high surface sensitivity. More details about this method are given in ref. 30.

3. Results and discussion

3.1. Bimetallic interactions in Pt@Rh core@shell nanoparticles

First, we investigated the evolution of the chemical states of the Pt core and the Rh shell in the Pt@Rh core@shell nanoparticles supported on Co$_3$O$_4$(111) as a function of temperature. The Pt 4f and Rh 3d core level spectra obtained after the preparation of the Pt@Rh/Co$_3$O$_4$(111) system are shown in Fig. 1a and b (bottom spectra), respectively. Two doublets are observed in the Pt 4f spectrum at 71.33 eV (Pt 4f$_{7/2}$) and 72.30 eV (Pt 4f$_{7/2}$)

(Fig. 1a, bottom spectrum). The dominant feature at 71.33 eV is attributed to metallic Pt^0 nanoparticles,[32] while the higher binding energy component at 72.30 eV has previously been assigned to the joint contribution from atomically dispersed Pt^{2+} species and ultra-small Pt$^{\delta+}$ aggregates on Co$_3$O$_4$(111).[17,32] In the Rh 3d spectrum (Fig. 1b, bottom spectrum), two doublets appear at 307.33 eV (Rh 3d$_{5/2}$) and 308.40 eV (Rh 3d$_{5/2}$), corresponding to metallic Rh^0 nanoparticles[19] and atomically dispersed Rh^{3+} species,[19] respectively.

The evolution of the Pt 4f and Rh 3d spectra during annealing in UHV is shown in Fig. 1a and b, respectively. The integrated intensities of the corresponding species are plotted in Fig. 1c as functions of temperature. Both Pt^{2+}/Pt$^{\delta+}$ and Pt^0 contributions remain fairly stable up to 400 K, indicating that the Pt core is stable within this temperature range. Between 400 and 500 K, the Pt^{2+}/Pt$^{\delta+}$ contribution decreases while the metallic Pt^0 increases, without a significant loss in total Pt 4f

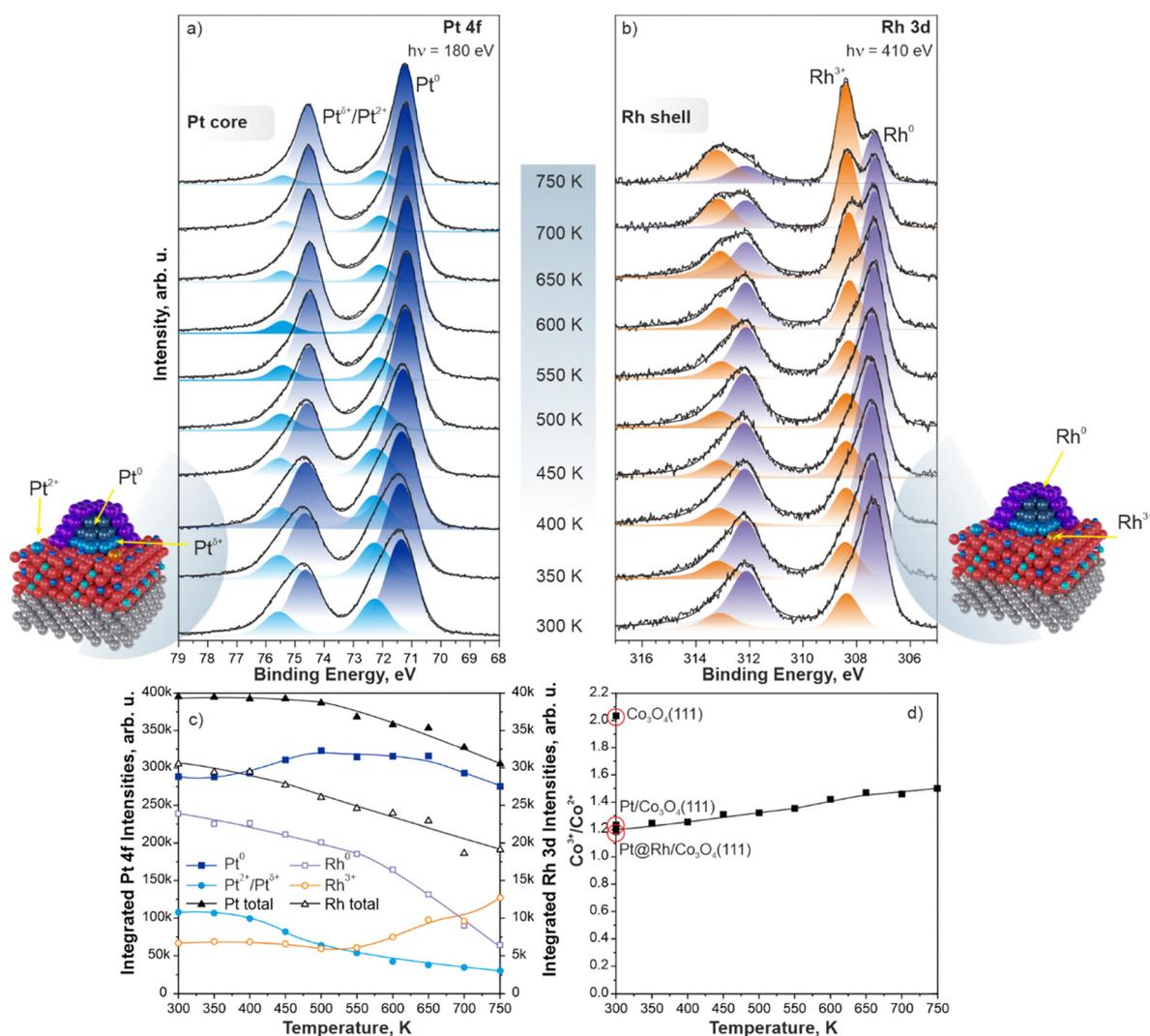**Fig. 1** Pt 4f and Rh 3d core level spectra (a) and (b), the evolution of the integrated Pt 4f and Rh 3d intensities (c), and the Co^{3+}/Co^{2+} ratio (d) obtained from the Pt@Rh/Co$_3$O$_4$(111) system as a function of temperature. The Pt 4f and Rh 3d core level spectra were acquired with photon energies of 180 and 410 eV, respectively.

This journal is © the Owner Societies 2026

Phys. Chem. Chem. Phys., 2026, **28**, 3675–3681 | **3677**

intensity. This behavior suggests the reduction of $Pt^{2+}/Pt^{\delta+}$ species to Pt^0 without substantial restructuring of the Pt core. Further annealing above 500 K leads to a gradual decrease in the total Pt signal, consistent with Pt sintering. Thus, the temperature range of 300–500 K can be identified as a region of structural stability of the Pt core. In the same temperature region, Rh^{3+} species remain stable, whereas Rh^0 decreases slightly. Such changes may indicate atomic ordering in the Rh shell, *e.g.*, faceting. During this process, a fraction of Rh atoms migrate toward the Pt core, causing a decrease in total Rh intensity. Above 550 K, Rh^0 is progressively oxidized to Rh^{3+}, and the total Rh signal decreases more sharply, suggesting sintering. Notably, both total Pt and Rh signals decrease in parallel during this process, implying that the core@shell structure of the Pt@Rh nanoparticles remains at least partially preserved during sintering. This behavior stands in sharp contrast to that observed earlier for Pd–Rh core–shell nanoparticles, where the total Pd signal decreased while the total Rh signal remained constant, indicating disintegration of the core@shell structure into separate Pd and Rh nanoparticles.[19]

Charge transfer between the Pt@Rh nanoparticles and the substrate was monitored *via* the Co^{3+}/Co^{2+} ratio (Fig. 1d). Pristine $Co_3O_4(111)$ exhibits a Co^{3+}/Co^{2+} ratio slightly above the nominal value of 2.0. This slight deviation is caused by adsorption of residual water.[17] After deposition of the Pt core, the ratio decreases to 1.2, indicating electron transfer from Pt to the substrate. Subsequent deposition of the Rh shell results in a further, minor decrease in the ratio. During annealing, the Co^{3+}/Co^{2+} ratio gradually increases, indicating progressive re-oxidation of the $Co_3O_4(111)$ substrate. The processes responsible for this re-oxidation have distinct origins. First, re-oxidation of $Co_3O_4(111)$ between 400 and 500 K is associated with the reduction of $Pt^{2+}/Pt^{\delta+}$ species to the metallic Pt^0 state. Second, re-oxidation of $Co_3O_4(111)$ above 500 K arises from charge dissipation deeper into the substrate.[19] We have previously observed this phenomenon in systems containing Rh and Pd–Rh core–shell nanoparticles on $Co_3O_4(111)$.[19] In those systems, charge dissipation was accompanied by disintegration of Rh^0 nanoparticles into Rh^{3+} species, followed by their diffusion into the $Co_3O_4(111)$ substrate.

3.2. Bimetallic interactions in Rh@Pt core@shell nanoparticles

Next, we examined the evolution of the chemical states of the Rh core and the Pt shell in the Rh@Pt core@shell nanoparticles supported on $Co_3O_4(111)$ as a function of temperature. The Rh 3d and Pt 4f core level spectra obtained after the preparation of the Rh@Pt/$Co_3O_4(111)$ system are shown in Fig. 2a and b (bottom spectra), respectively.

Similar to the Pt@Rh system, two doublets are observed in the Rh 3d spectrum at 307.70 eV (Rh $3d_{5/2}$) and 308.80 eV (Rh $3d_{5/2}$), corresponding to metallic Rh^0 and atomically dispersed Rh^{3+} species, respectively. Likewise, two doublets appear in the Pt 4f spectrum at 71.35 eV (Pt $4f_{7/2}$) and 72.34 eV (Pt $4f_{7/2}$). The dominant contribution at 71.35 eV is assigned to metallic Pt^0, while the higher binding energy peak at 72.34 eV is attributed to the joint contribution of $Pt^{2+}/Pt^{\delta+}$ species. The evolution of the Rh 3d and Pt 4f core level spectra during annealing in UHV is shown in Fig. 2a and b, respectively. The integrated intensities of the corresponding species are plotted in Fig. 2c as functions of temperature. The annealing induces changes in both the Rh 3d and Pt 4f spectra of the Rh@Pt nanoparticles, similar to those observed for Pt@Rh/$Co_3O_4(111)$. The Rh core remains stable up to 400 K, after which distinct changes become apparent. At 450 K, the total Rh intensity increases sharply, driven by an increase in the metallic Rh^0 contribution. This is caused by the reduction of Rh^{3+} species and their subsequent migration onto the Rh@Pt nanoparticles. The reduction of Rh^{3+} to Rh^0 extends up to 500 K, but it no longer leads to the increase in total Rh intensity. On the contrary, we observed a decrease in total Rh intensity. This observation suggests that Rh^0 atoms migrate toward the Rh core. In the same temperature range (400–500 K), the reduction of $Pt^{2+}/Pt^{\delta+}$ to Pt^0 occurs similarly to that observed for the Pt@Rh nanoparticles. However, the trend in the evolution of the Pt^0 contribution differs slightly, likely due to Rh atoms migrating onto the Pt shell. Above 500 K, strong oxidation of Rh^0 to Rh^{3+} occurs, accompanied by diffusion of Rh^{3+} species into the $Co_3O_4(111)$ substrate.

The observed behavior indicates that the Rh@Pt nanoparticles remain fairly structurally stable up to 500 K. Nevertheless, despite partial disintegration of the Rh core above 500 K, the total Rh intensity decreases in parallel with the total Pt intensity. This observation suggests that the Rh@Pt nanoparticles undergo sintering without phase separation into individual Rh and Pt nanoparticles.

Charge transfer was again probed *via* the Co^{3+}/Co^{2+} ratio (Fig. 2d). Pristine $Co_3O_4(111)$ shows a ratio of $\sim$2.1, slightly above the stoichiometric value of 2.0, due to co-adsorption of residual water.[17] Deposition of the Rh core leads to reduction of the $Co_3O_4(111)$ substrate, yielding a Co^{3+}/Co^{2+} ratio of 1.5. Subsequent deposition of the Pt shell causes further reduction, resulting in a Co^{3+}/Co^{2+} ratio of 1.2. Upon annealing, a gradual re-oxidation of $Co_3O_4(111)$ is observed. This process results from the reduction of $Pt^{2+}/Pt^{\delta+}$ and Rh^{3+} species to Pt^0 and Rh^0, respectively, below 500 K, and from charge dissipation into the substrate above 500 K.

3.3. Modulation of the EMSI by means of Rh–Pt bimetallic interactions

Finally, we analyzed the binding energy shifts of the Rh $3d_{5/2}$ and Pt $4f_{7/2}$ core levels for Pt@Rh/$Co_3O_4(111)$ and Rh@Pt/$Co_3O_4(111)$ relative to the reference monometallic Rh/$Co_3O_4(111)$ and Pt/$Co_3O_4(111)$ systems as a function of the annealing temperature (Fig. 3a and b).

The evolutions of the oxidation states of Rh and Pt nanoparticles in the reference monometallic Rh/$Co_3O_4(111)$ and Pt/$Co_3O_4(111)$ systems have been investigated in detail previously.[19,32] Briefly, the metallic Rh^0 contribution exhibits a binding energy of 307.30 eV (Rh $3d_{5/2}$) for 1.9 ML Rh nanoparticles deposited at 300 K.[19] During annealing in UHV, this contribution maintains its binding energy nearly constant up to
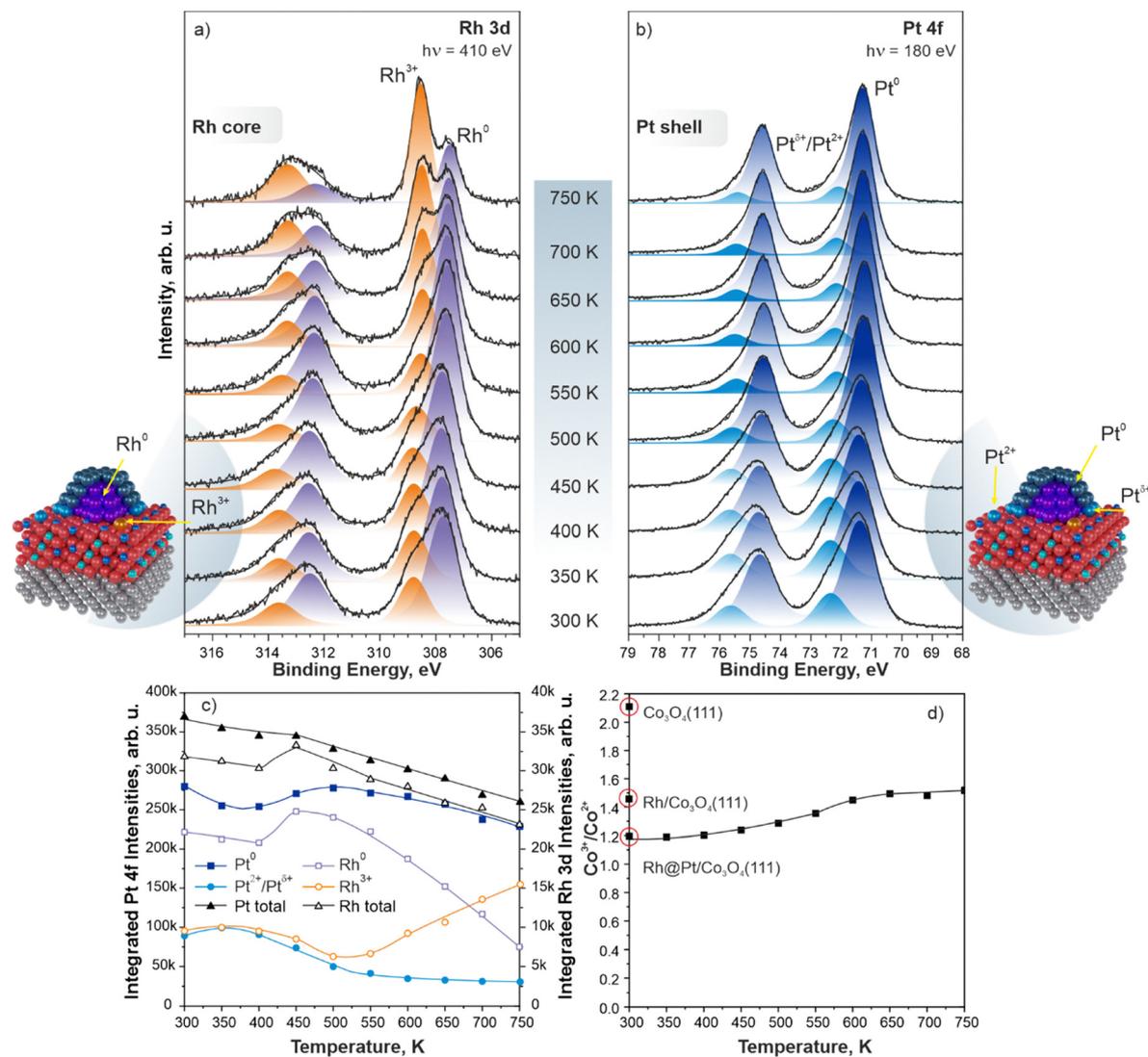
3678 | *Phys. Chem. Chem. Phys.*, 2026, **28**, 3675–3681

This journal is © the Owner Societies 2026

Fig. 2 Rh 3d and Pt 4f core level spectra (a) and (b), the evolution of the integrated Rh 3d and Pt 4f intensities (c) and the Co^{3+}/Co^{2+} (d) obtained from the Rh@Pt/Co_3O_4(111) system as a function of temperature. The Rh 3d and Pt 4f core level spectra were acquired with 410 and 180 eV photon energy, respectively.

500 K. However, above 500 K, we observed a pronounced shift of the Rh^0 contribution toward higher binding energy, reaching 307.60 eV at 750 K. This shift is consistent with a partial oxidation of Rh nanoparticles due to electron transfer from Rh to the support.

This behavior contrasts sharply with that of Pt^0 contribution in the reference Pt/Co_3O_4(111) system.[32] For 1.3 ML Pt nanoparticles deposited at 300 K, the Pt^0 contribution appears at 71.35 eV (Pt $4f_{7/2}$) and remains unchanged up to 400 K. Above this temperature, the Pt^0 contribution gradually shifts to lower binding energies, reaching 71.15 eV at 750 K. This trend indicates partial reduction of Pt nanoparticles, driven by electron transfer from the support to Pt. The opposite directions of charge transfer upon annealing, *i.e.*, oxidation for Rh and reduction for Pt, are characteristic of these two metals supported on Co_3O_4(111).

Interestingly, these counteracting electronic behaviors manifest simultaneously in the Rh–Pt core–shell nanoparticles.

At 300 K, the Rh^0 binding energies are 307.33 eV for Pt@Rh and 307.70 eV for Rh@Pt nanoparticles. These differences reflect distinct degrees of charge transfer between Rh and Co_3O_4(111). The higher binding energy of the Rh core contribution in Rh@Pt nanoparticles arises from its direct contact with the Co_3O_4(111). The lower binding energy of the Rh shell contribution results from the absence of direct Rh–Co_3O_4(111) contact in the Pt@Rh nanostructure. Below 500 K, the evolution of the Rh $3d_{5/2}$ binding energy of the Rh^0 contributions in both Pt@Rh and Rh@Pt nanoparticles follows the same trend observed for monometallic Rh nanoparticles. Remarkably, above 500 K, this trend reverses: the binding energies of Rh^0 contributions in both Pt@Rh and Rh@Pt nanoparticles remain essentially constant upon annealing up to 750 K. This stabilization indicates that the Rh–Pt bimetallic interaction effectively counteracts EMSI-driven oxidation, maintaining the metallic character of Rh even at elevated temperatures.
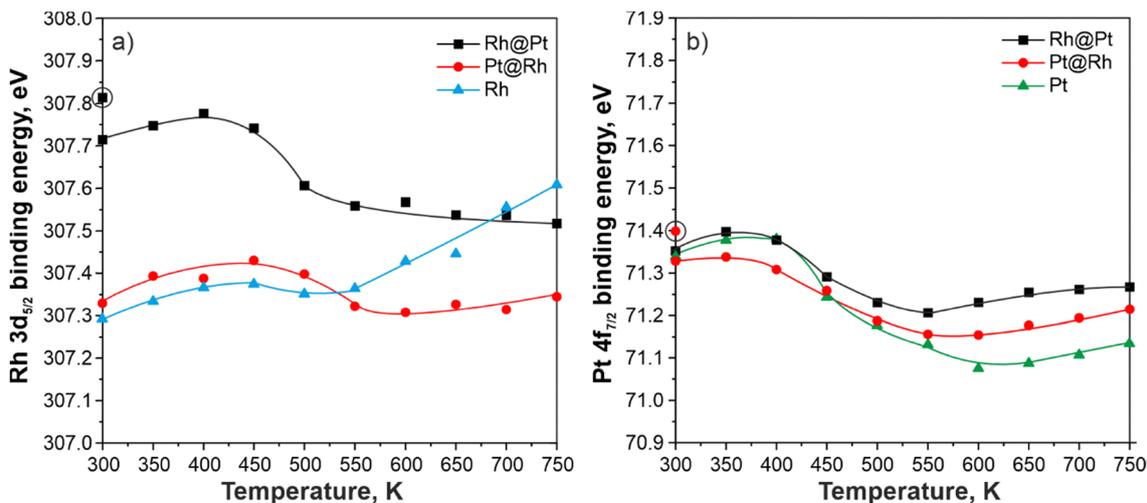
This journal is © the Owner Societies 2026

Phys. Chem. Chem. Phys., 2026, 28, 3675–3681 | 3679

Fig. 3 Rh $3d_{5/2}$ and Pt $4f_{7/2}$ binding energies of metallic Rh^0 and Pt^0 contributions (a and b) for Rh@Pt and Pt@Rh core@shell nanoparticles as well as for reference monometallic Rh and Pt nanoparticles as a function of temperature. The data for the reference monometallic Rh and Pt nanoparticles are obtained by analysis of Rh 3d and Pt 4f spectra published in ref. 19 and 32. The data points in circles indicate the Rh $3d_{5/2}$ binding energy of the Rh core before deposition of Pt shell in the Rh@Pt (a) and the Pt $4f_{7/2}$ binding energy of the Pt core before deposition of Rh shell in the Pt@Rh nanoparticles (b).

For both Pt@Rh and Rh@Pt nanoparticles, the Pt $4f_{7/2}$ binding energies of the Pt^0 contributions at 71.35 eV (Pt $4f_{7/2}$) are similar to those observed for the monometallic Pt nanoparticles (Fig. 3b). Also, the Pt $4f_{7/2}$ binding energy of the Pt^0 contributions from the bimetallic Pt@Rh and Rh@Pt structures exhibit generally similar trends to that of the monometallic Pt nanoparticles with increasing temperature.

Generally, we attribute strong stabilization of the metallic character of Rh in the Pt@Rh and Rh@Pt core@shell nanoparticles to the intrinsic tendency of Rh and Pt to form stoichiometric intermetallic compounds.[23] In contrast, Rh–Pd phase equilibria exhibit a miscibility gap within the studied composition and temperature ranges.[24] Furthermore, theoretical predictions confirm the immiscibility of Rh and Pd in nanoparticles, particularly near a 1:1 composition, regardless of particle size.[25] The lack of such miscibility in Rh–Pd systems explains their tendency toward phase separation, whereas the Rh–Pt system benefits from strong bimetallic interaction and alloying, which suppresses disintegration and oxidation upon annealing.

4. Conclusions

We have investigated how bimetallic Rh–Pt interactions influence the extent of the EMSI between Rh and the $Co_3O_4(111)$ substrate using SRPES. The results demonstrate that the bimetallic interaction within Rh–Pt core–shell nanoparticles mitigates the strength of the EMSI, thereby preserving the metallic character of Rh in both Pt@Rh and Rh@Pt core@shell nanostructures.

Both Pt@Rh and Rh@Pt core–shell nanoparticles predominantly consist of metallic Rh^0 and Pt^0 species. These are accompanied by minor amounts of atomically dispersed Rh^{3+} and Pt^{2+}, as well as ultrasmall $Pt^{\delta+}$ aggregates. Upon annealing below 500 K, partial reduction of the oxidized Rh^{3+} and $Pt^{2+}/Pt^{\delta+}$

species occurs, while the overall core@shell structure remains stable. Annealing above 500 K induces partial oxidation of the Rh shell in Pt@Rh and the Rh core in Rh@Pt nanostructures. This is followed by diffusion of Rh^{3+} species into the $Co_3O_4(111)$ substrate. This process is accompanied by sintering of Pt@Rh and Rh@Pt core@shell nanoparticles but notably proceeds without significant phase separation.

Overall, these findings reveal that Rh–Pt bimetallic interactions effectively counteract EMSI-induced oxidation and disintegration of the bimetallic phase. The results provide fundamental insight into how bimetallic design can regulate interfacial charge transfer and structural stability at metal/oxide interfaces, offering guiding principles for the rational design of electronically balanced and thermally stable noble metal catalysts supported on reducible oxides.

Author contributions

Jonas Hauner: formal analysis, investigation, visualization, writing – original draft. Alexander Simanenko: investigation, writing – review & editing. Lukáš Fusek: investigation, writing – review & editing. Tomáš Skála: investigation, writing – review & editing. Nataliya Tsud: investigation, writing – review & editing. Firas Faisal: investigation, writing – review & editing. Sascha Mehl: investigation, writing – review & editing. Jörg Libuda: conceptualization, writing – review & editing. Yaroslava Lykhach: conceptualization, visualization, investigation, project administration, supervision, writing – review & editing, funding acquisition.

Conflicts of interest

There are no conflicts to declare.

3680 | *Phys. Chem. Chem. Phys.*, 2026, **28**, 3675–3681

This journal is © the Owner Societies 2026

Data availability

Data for this article are available at Zenodo at https://doi.org/10.5281/zenodo.17749350.

Supplementary information (SI): LEED patterns obtained from Co_3O_4(111) thin films grown on Ir(100) substrates before deposition of Pt@Rh and Rh@Pt core@shell nanoparticles. See DOI: https://doi.org/10.1039/d5cp04654h.

Acknowledgements

References

1 A. Bruix, J. A. Rodriguez, P. J. Ramírez, S. D. Senanayake, J. Evans, J. B. Park, D. Stacchiola, P. Liu, J. Hrbek and F. Illas, *J. Am. Chem. Soc.*, 2012, **134**, 8968–8974.

2 C. T. Campbell, *Nat. Chem.*, 2012, **4**, 597–598.

3 T. W. van Deelen, C. Hernández Mejía and K. P. de Jong, *Nat. Catal.*, 2019, **2**, 955–970.

4 Y. Lykhach, S. M. Kozlov, T. Skála, A. Tovt, V. Stetsovych, N. Tsud, F. Dvořák, V. Johánek, A. Neitzel, J. Mysliveček, S. Fabris, V. Matolín, K. M. Neyman and J. Libuda, *Nat. Mater.*, 2016, **15**, 284–288.

5 D. Leybo, U. J. Etim, M. Monai, S. R. Bare, Z. Zhong and C. Vogt, *Chem. Soc. Rev.*, 2024, **53**, 10450–10490.

6 K. Sang, J. Zuo, X. Zhang, Q. Wang, W. Chen, G. Qian and X. Duan, *Green Energy Environ.*, 2023, **8**, 619–625.

7 Y. Li, Y. Zhang, K. Qian and W. Huang, *ACS Catal.*, 2022, **12**, 1268–1287.

8 G. Pacchioni, *Phys. Chem. Chem. Phys.*, 2013, **15**, 1737–1757.

9 G. Pacchioni and H.-J. Freund, *Chem. Soc. Rev.*, 2018, **47**, 8474–8502.

10 P. Castro-Latorre, K. M. Neyman and A. Bruix, *J. Phys. Chem. C*, 2023, **127**, 17700–17710.

11 A. Bruix, Y. Lykhach, I. Matolínová, A. Neitzel, T. Skála, N. Tsud, M. Vorokhta, V. Stetsovych, K. Ševčíková, J. Mysliveček, R. Fiala, M. Václavů, K. C. Prince, S. Bruyere, V. Potin, F. Illas, V. Matolín, J. Libuda and K. M. Neyman, *Angew. Chem., Int. Ed.*, 2014, **53**, 10525–10530.

12 M. Farnesi Camellone, F. Dvořák, M. Vorokhta, A. Tovt, I. Khalakhan, V. Johánek, T. Skála, I. Matolínová, S. Fabris and J. Mysliveček, *ACS Catal.*, 2022, **12**, 4859–4871.

13 R. Lang, W. Xi, J.-C. Liu, Y.-T. Cui, T. Li, A. F. Lee, F. Chen, Y. Chen, L. Li, L. Li, J. Lin, S. Miao, X. Liu, A.-Q. Wang, X. Wang, J. Luo, B. Qiao, J. Li and T. Zhang, *Nat. Commun.*, 2019, **10**, 234.

14 F. Kraushofer, L. Haager, M. Eder, A. Rafsanjani-Abbasi, Z. Jakub, G. Franceschi, M. Riva, M. Meier, M. Schmid, U. Diebold and G. S. Parkinson, *ACS Energy Lett.*, 2022, **7**, 375–380.

15 Z. Jakub, J. Hulva, M. Meier, R. Bliem, F. Kraushofer, M. Setvin, M. Schmid, U. Diebold, C. Franchini and G. S. Parkinson, *Angew. Chem., Int. Ed.*, 2019, **58**, 13961–13968.

16 F. Kraushofer and G. S. Parkinson, *Chem. Rev.*, 2022, **122**, 14911–14939.

17 L. Fusek, M. Farnesi Camellone, M. Ronovský, M. Kastenmeier, T. Skála, P. K. Samal, N. Tsud, S. Mehl, J. Škvára, T. Dolák, V. Uvarov, M. Setvín, V. Johánek, S. Fabris, O. Brummel, J. Libuda, J. Mysliveček, S. Piccinin and Y. Lykhach, *J. Mater. Chem. A*, 2024, **12**, 3258–3264.

18 F. Faisal, C. Stumm, M. Bertram, F. Waidhas, Y. Lykhach, S. Cherevko, F. Xiang, M. Ammon, M. Vorokhta, B. Šmíd, T. Skála, N. Tsud, A. Neitzel, K. Beranová, K. C. Prince, S. Geiger, O. Kasian, T. Wähler, R. Schuster, M. A. Schneider, V. Matolín, K. J. J. Mayrhofer, O. Brummel and J. Libuda, *Nat. Mater.*, 2018, **17**, 592–598.

19 A. Simanenko, J. Škvára, P. K. Samal, L. Fusek, M. Kastenmeier, M. Ronovský, T. Skála, N. Tsud, S. Mehl, V. Johánek, J. Mysliveček, O. Brummel, Y. Lykhach and J. Libuda, *J. Phys. Chem. C*, 2025, **129**, 983–992.

20 A. Simanenko, J. Škvára, P. K. Samal, E. Franz, R. Hübsch, T. Skála, N. Tsud, S. Mehl, D. Schauermann, V. Johánek, J. Mysliveček, O. Brummel, Y. Lykhach and J. Libuda, *Nanoscale*, 2025, **17**, 11679–11690.

21 S. Lyu, D. Zhao, H. Zhang, H. Li, F. Wen, Q. Zhou, R. Zhang, Y. Wu, C. Hou, G. Xia, R. Xu and X. Li, *Carbon Capture Sci. Technol.*, 2025, **14**, 100381.

22 D. Yuan, Z. Hu, Z. Chen, J. Liu, J. Sun, Y. Song, S. Dong and L. Zhang, *J. Phys. Chem. Lett.*, 2024, **15**, 3486–3492.

23 H. Okamoto, *J. Phase Equilib. Diffus.*, 2013, **34**, 176–177.

24 S. N. Tripathi and S. R. Bharadwqj, *J. Phase Equilib.*, 1994, **15**, 208–212.

25 L. Vega, H. A. Aleksandrov and K. M. Neyman, *Chin. J. Catal.*, 2019, **40**, 1749–1757.

26 G. Rupprechter, Surface Science Approach to Heterogeneous Catalysis, *Surf. Interface Sci.*, 2016, **5**, 459–528.

27 W. Meyer, K. Biedermann, M. Gubo, L. Hammer and K. Heinz, *J. Phys.: Condens. Matter*, 2008, **20**, 265011.

28 K. Biedermann, M. Gubo, L. Hammer and K. Heinz, *J. Phys.: Condens. Matter*, 2009, **21**, 185003.

29 K. Heinz and L. Hammer, *J. Phys.: Condens. Matter*, 2013, **25**, 173001.

30 M. Kastenmeier, L. Fusek, F. Mohamed, C. Schuschke, M. Ronovský, T. Skála, M. Farnesi Camellone, N. Tsud, V. Johánek, S. Fabris, J. Libuda, S. Piccinin, Y. Lykhach, J. Mysliveček and O. Brummel, *J. Phys. Chem. C*, 2023, **127**, 6034–6044.

31 H.-P. Feng, L. Tang, G.-M. Zeng, Y. Zhou, Y.-C. Deng, X. Ren, B. Song, C. Liang, M.-Y. Wei and J.-F. Yu, *Adv. Colloid Interface Sci.*, 2019, **267**, 26–46.

32 Y. Lykhach, F. Faisal, T. Skála, A. Neitzel, N. Tsud, M. Vorokhta, F. Dvořák, K. Beranová, Y. Kosto, K. C. Prince, V. Matolín and J. Libuda, *J. Mater. Chem. A*, 2018, **6**, 23078–23086.

33 J. Libra, *KolXPD: Spectroscopy Data Measurement and Processing*, https://www.kolibrik.net/science/kolxpd/, (accessed 1.09.2025).

This journal is © the Owner Societies 2026

Phys. Chem. Chem. Phys., 2026, **28**, 3675–3681 | **3681**